

STSR-INR: Spatiotemporal Super-Resolution for Multivariate Time-Varying Volumetric Data via Implicit Neural Representation

Kaiyuan Tang^a, Chaoli Wang^a

^aDepartment of Computer Science and Engineering, University of Notre Dame, Notre Dame, IN 46556, United States

ARTICLE INFO

Article history:

Received November 26, 2023

Keywords: Spatiotemporal super-resolution, implicit neural representation, multivariate time-varying data

ABSTRACT

Implicit neural representation (INR) has surfaced as a promising direction for solving different scientific visualization tasks due to its continuous representation and flexible input and output settings. We present STSR-INR, an INR solution for generating simultaneous spatiotemporal super-resolution for multivariate time-varying volumetric data. Inheriting the benefits of the INR-based approach, STSR-INR supports unsupervised learning and permits data upscaling with arbitrary spatial and temporal scale factors. Unlike existing GAN- or INR-based super-resolution methods, STSR-INR focuses on tackling variables or ensembles and enabling joint training across datasets of various spatiotemporal resolutions. We achieve this capability via a variable embedding scheme that learns latent vectors for different variables. In conjunction with a modulated structure in the network design, we employ a variational auto-decoder to optimize the learnable latent vectors to enable latent-space interpolation. To combat the slow training of INR, we leverage a multi-head strategy to improve training and inference speed with significant speedup. We demonstrate the effectiveness of STSR-INR with multiple scalar field datasets and compare it with conventional tricubic+linear interpolation and state-of-the-art deep-learning-based solutions (STNet and CoordNet).

© 2023 Elsevier B.V. All rights reserved.

1. Introduction

In many applications, domain scientists run large-scale simulations to generate spatiotemporal multivariate volumetric data for analyzing the corresponding physical or chemical processes. These simulations often come with various conditions, settings, or configurations, leading to multiple runs. The resulting multivariate or ensemble data are different but usually share a similar structural appearance. Analyzing and visualizing such high-dimensional spatiotemporal data requires enormous disk and memory storage for post hoc analysis, presenting a significant challenge to domain experts and visualization researchers.

One way to tame the high storage cost is to save only downsampled low-resolution data and then apply spatiotemporal super-resolution (STSR) techniques to recover their high-resolution counterparts. For instance, given a downsampled volume sequence (e.g., 50 timesteps with 128^3 spatial resolution),

the STSR task aims to upsample the sequence to a high-resolution one (e.g., 150 timesteps with 512^3 spatial resolution). Over the past few years, we have witnessed a surge of deep-learning-based solutions for accomplishing many scientific visualization tasks, including super-resolution generation [1]. For the end-to-end STSR generation, STNet [2] and STSRNet [3] are state-of-the-art examples that upscale volumetric scalar and vector data, respectively. Nevertheless, both works suffer significant limitations.

First, these solutions are based on convolutional neural networks (CNNs) and generative adversarial networks (GANs). Due to their *discrete, resolution-dependent* network designs, CNN and GAN-based STSR solutions demand ground-truth (GT) high-resolution data during training in a supervised manner. They cannot interpolate arbitrarily-resolved spatial or temporal resolution.

17
18
19
20
21
22
23
24
25

26
27
28
29
30
31
32

1 Second, neither STSR method provides sound guidance for
 2 training *multivariate* or *ensemble* datasets. They tackle each
 3 variable or ensemble sequence as an independent training pro-
 4 cess, making similar structure learning redundant. One straight-
 5 forward way to achieve multivariate STSR is to expand the net-
 6 work’s output, i.e., inferring multiple variables simultaneously.
 7 This calls for an increased network capacity, which may not
 8 always be desirable. Moreover, the variation of variable or en-
 9 semble distributions could negatively impact each other during
 10 training, leading to performance degradation.

11 Third, moving from different variables to *different datasets*,
 12 both STNet and STSRNet do not permit joint training of dif-
 13 ferent datasets of various spatiotemporal resolutions. For flex-
 14 ibility and efficiency, it is ideal that the same network trains
 15 multiple datasets simultaneously without sacrificing inference
 16 quality. However, such a joint training scheme has not been
 17 thoroughly studied in scientific visualization for the STSR task.

18 To respond, we design STSR-INR, spatiotemporal super-
 19 resolution via implicit neural representation. Unlike CNN or
 20 GAN, INR ingests coordinates and predicts quantities of inter-
 21 est via a neural network, commonly in the form of *multilayer*
 22 *perceptrons* (MLPs) or *fully-connected network* (FCN). With
 23 INR, the memory required to parameterize the signal depends
 24 on its *complexity* rather than *resolution*. We leverage such an
 25 FCN to learn a *continuous* representation from *discrete* data
 26 samples. Doing so brings two benefits. First, it can achieve
 27 *unsupervised learning*, which does not need seeing low- and
 28 high-resolution volume pairs for training. Second, it supports
 29 upsampling the input low-resolution volume sequence to an *ar-
 30 bitrary spatial or temporal scale* without modifying network
 31 structure or retraining.

32 To help the network learn multivariate sequences, we design
 33 a *variable embedding* scheme along with a *modulated structure*
 34 to optimize each variable independently while utilizing their
 35 shared structural appearance for training. Variable embedding
 36 models each variable or ensemble sequence as a *learnable lat-
 37 ent vector*, enabling the network to capture more detailed vari-
 38 able variations. To better utilize the latent vector, we devise a
 39 modulated structure consisting of a *modulator network* and a
 40 *synthesis network*. The modulator network will provide the lat-
 41 ent vector with more control over the feature map in the syn-
 42 thesis network and, thus, could improve the quality of synthesized
 43 spatiotemporal volumes. This embedding structure is highly
 44 flexible and can support the joint training of different datasets
 45 of various spatiotemporal resolutions within the same network.
 46 Furthermore, our variable embedding is learned with a *vari-
 47 ational auto-decoder*, which optimizes the latent vector, allow-
 48 ing us to conduct latent-space interpolation. Finally, INR-based
 49 solutions are notoriously slow in training as an entire feedfor-
 50 ward pass through the network must be computed for each sam-
 51 ple. We utilize a *multi-head strategy* to boost the training and
 52 inference speed of STSR-INR significantly.

53 We experiment with STSR-INR on several multivariate or
 54 ensemble scalar field datasets and compare it against tricu-
 55 bic+linear interpolation, GAN-based STNet [2], and INR-based
 56 CoordNet [4]. The results demonstrate that STSR-INR achieves
 57 competitive quality on most datasets using data-, image-, and

58 feature-level metrics. The contribution of this paper is as fol-
 59 lows. First, we present the design of STSR-INR, a novel INR-
 60 based solution to achieve STSR for multivariate or ensemble
 61 spatiotemporal volume data. Second, we experiment with the
 62 multi-head strategy to effectively tackle the issue of slow train-
 63 ing with INR. Third, we investigate the utility of our embed-
 64 ding structure via joint training, latent-space interpolation, and
 65 network analysis. Fourth, we show the advantages of STSR-
 66 INR over the state-of-the-art STSR solutions based on GAN
 67 and INR. Finally, we investigate two key network settings for
 68 STSR-INR and study their impacts on performance.

2. Related work

69 This section discusses related works of deep learning for sci-
 70 entific visualization, super-resolution generation, and INR tech-
 71 niques.

2.1. Deep Learning for Scientific Visualization

72 There is an exciting trend of leveraging deep-learning-based
 73 methods for solving scientific visualization tasks, including
 74 data generation, visualization generation, prediction, object
 75 detection and segmentation, and feature learning and extrac-
 76 tion [1]. Among them, the task most relevant to this work is
 77 *data generation*, which aims to infer or reconstruct new ver-
 78 sions of data from existing versions or their reduced visual
 79 representations. The most popular form of data generation
 80 is *super-resolution generation*, which uses downsampled low-
 81 resolution data to produce high-resolution versions [5]. For
 82 instance, Han and Wang designed SSR-TVD [6], which ap-
 83 plies a GAN to upscale the low-resolution 3D volumetric se-
 84 quences into high-resolution ones. Another form of data gener-
 85 ation is *data reconstruction*, which infers the original data from
 86 their visual representations. For example, Gu et al. [7] con-
 87 sidered the problem of reconstructing unsteady flow data from
 88 their reduced visual forms: a set of representative streamlines.
 89 Their VFR-UFD solution can recover high-quality vector data
 90 from these compact streamlines via a diffusion step followed by
 91 deep-learning-based denoising. The third form of data genera-
 92 tion is *data translation*, i.e., ingesting one variable or ensemble
 93 sequence to infer another sequence, commonly called variable-
 94 to-variable (V2V) translation [8]. For instance, Scalar2Vec [9]
 95 translates one scalar field to its corresponding velocity vector
 96 field using the k -complete bipartite translation network.

97 In this work, we focus on spatiotemporal super-resolution
 98 generation. Given low spatial and temporal resolution volume
 99 sequences, we aim to upscale them to high spatial and temporal
 100 resolution ones in an end-to-end fashion, similar to STNet [2].
 101 Unlike vector field STSR model STSRNet [3], STSR-INR is
 102 designed for scalar field multivariate time-varying data and
 103 does not upscale vector field data or include motion estimation
 104 for flow field reconstruction. One of the concurrent works is
 105 FFEINR [10], which employs INR to achieve STSR for flow
 106 field data with fast training and inference speed. In contrast to
 107 FFEINR, which utilizes an encoder to extract the downsampled
 108 data features, our STSR-INR embeds features through a series
 109 of learnable latent vectors and thus could maintain a relatively
 110 lightweight architecture.

2.2. Super-Resolution Generation

Super-resolution techniques transform low-resolution data into high-resolution versions, including spatial super-resolution (SSR), temporal super-resolution (TSR), and STSR. Examples of deep-learning-based SSR works are SRCNN [11], SRFBN [12], and SwinIR [13], which solve the inference of high-resolution details in the spatial domain. TSR takes subsampled time sequences to interpolate intermediate timesteps with the same spatial resolution. Example works include phase-based interpolation [14], SepConv [15], and SloMo [16]. SSR and TSR only focus on the spatial or temporal domain, but not both. STSR addresses both spatial and temporal super-resolution simultaneously. Compared with conventional interpolation methods, deep-learning-based methods can reconstruct more accurate results because of their ability to fit complex global patterns of the target data.

Our work falls into the STSR category. Previous methods, like STNet [2], can only upsample the input data with a *fixed* spatial or temporal scale factor. On the contrary, our STSR-INR can upscale the input low-resolution data to an *arbitrary* scale, thanks to the *continuous* neural representation of spatial and temporal domains. Moreover, STSR-INR accomplishes spatial and temporal upscaling in an *unsupervised* manner. This means that, unlike STNet, STSR-INR does not keep low- and high-resolution volume pairs or the complete subsequence of early timesteps for training optimization.

2.3. INR-Based Techniques

Recent works have investigated utilizing MLPs or FCNs to learn the continuous INR from discrete data samples. The most notable works are neural radiance field (NeRF) and sinusoidal representation network (SIREN). Mildenhall et al. [17] introduced NeRF, which applies an FCN with position encoding to learn the continuous volumetric scene and synthesize novel views. Sitzmann et al. [18] proposed SIREN that leverages the periodic activation function to help the MLPs learn the complex data signals more accurately. In scientific visualization, INR-based examples include neurcomp for neural compression of volume data [19], fV-SRN, a fast version of a scene representation network for volume rendering [20], neural flow map for particle trajectory prediction [21], and instant neural representation for interactive volume rendering [22].

Researchers have extracted feature information and injected it into the INR model's input to improve the performance and generalization ability. A direction is utilizing an encoder to extract latent features from subsampled data, often called the auto-encoder architecture. Example works in this direction include VideoINR [23] and ArSSR [24]. However, volumetric data are massive 4D space-time data, often demanding excessive GPU memory consumption when applying an encoder for feature extraction. Instead of using the *auto-encoder* architecture, we leverage the *auto-decoder* architecture, which derives the feature information by assigning each type of signal (e.g., variable or ensemble) a learnable latent vector and optimizing the latent vector together with deep network parameters in the training process. Works such as DeepSDF [25] and DyNeRF [26] fall into this category.

The work most closely related to our work is CoordNet [4], which leverages INR to achieve data generation (i.e., SSR and TSR) and visualization generation (i.e., view synthesis and ambient occlusion prediction) tasks. Our STSR-INR work also targets super-resolution generation via INR. However, it tackles SSR and TSR simultaneously. We make significant changes to the baseline CoordNet framework to efficiently and effectively handle super-resolution generation for multiple variables or ensembles, which has never been explored. Furthermore, instead of training each model to learn the representation of individual datasets, our work can train the same model to learn across multiple datasets with various spatiotemporal resolutions. A recent concurrent work that also adopts CoordNet is HyperINR [27], which employs hypernetwork to produce the weights of an INR. However, HyperINR mainly focuses on the TSR of one scalar dataset, while our STSR-INR processes STSR on a single multivariate dataset or across multiple datasets.

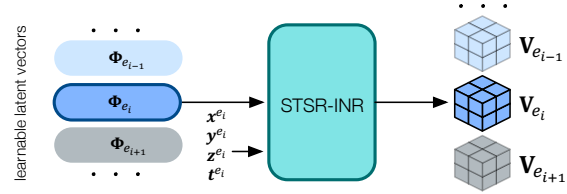


Fig. 1: Overview of STSR-INR. The network predicts the corresponding voxel value by inputting the variable-specific latent vector and space-time coordinates.

3. STSR-INR

3.1. Overview

Let $\mathbf{D} = \{\mathbf{D}_{e_1}, \mathbf{D}_{e_2}, \dots, \mathbf{D}_{e_n}\}$ be a set of n multivariate volume sequences, where \mathbf{D}_{e_i} is the volume sequence for variable or ensemble e_i and $\mathbf{e} = \{e_1, e_2, \dots, e_n\}$. $\mathbf{D}_{e_i} = \{\mathbf{C}_{e_i}, \mathbf{V}_{e_i}\}$ contains a set of input space-time coordinates $\mathbf{C}_{e_i} = \{(x_1^{e_i}, y_1^{e_i}, z_1^{e_i}, t_1^{e_i}), (x_2^{e_i}, y_2^{e_i}, z_2^{e_i}, t_2^{e_i}), \dots\}$ and their corresponding values $\mathbf{V}_{e_i} = \{v_1^{e_i}, v_2^{e_i}, \dots\}$. As sketched in Figure 1, to achieve simultaneous training over multiple variables, we design *variable embedding* that assigns each variable sequence \mathbf{D}_{e_i} a *learnable latent vector* Φ_{e_i} . During training, we aim to learn the mapping from \mathbf{C}_{e_i} conditioned on Φ_{e_i} to \mathbf{V}_{e_i} by updating both Φ_{e_i} and network parameters Θ . That is,

$$\mathcal{F}_{\Theta} : (\mathbf{C}; \Phi) \rightarrow \mathbf{V}, \quad (1)$$

where $\mathbf{C} = \{\mathbf{C}_{e_1}, \mathbf{C}_{e_2}, \dots, \mathbf{C}_{e_n}\}$, $\Phi = \{\Phi_{e_1}, \Phi_{e_2}, \dots, \Phi_{e_n}\}$, and $\mathbf{V} = \{\mathbf{V}_{e_1}, \mathbf{V}_{e_2}, \dots, \mathbf{V}_{e_n}\}$. Once the network is trained, given the optimized latent vector Φ_{e_i} , STSR-INR can predict \mathbf{V}_{e_i} from unseen intermediate spatial and temporal coordinates. For the STSR task, given the spatial and temporal upscale factors u_s and u_t , it can reconstruct volume sequences with higher spatial and temporal resolutions by inference on a scaled spatiotemporal grid.

3.2. Network Architecture

SIREN and skip-connection. As illustrated in the left of Figure 2, our STSR-INR is a SIREN-based [18] network which

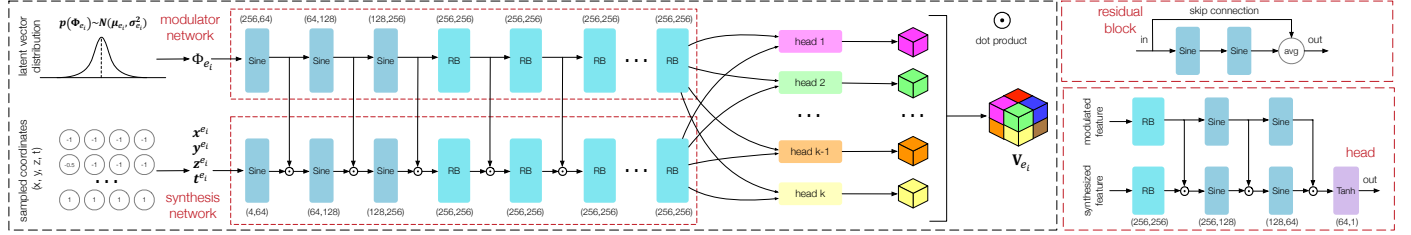


Fig. 2: Network structure of STSR-INR. Left: Overview of STSR-INR. The modulator network takes the sampled latent vector, and the synthesis network takes coordinates as input. The modulator then modulates the synthesis activations using dot products. Finally, each head in the multi-head structure reconstructs a subvolume of the same size in the whole volume. During training, we jointly optimize network and variable-specific latent vector distribution parameters. Top-right: Detailed structure of the residual block. Bottom-right: Detailed structure of the network’s head part.

1 consists of fully-connected layers and the Sine activation function. Compared with other activation functions like ReLU 2 or Tanh, employing Sine helps the network fit complex signals, especially high-frequency parts, more quickly and accurately. Moreover, if the input and output dimensions are consistent, we add skip-connection between every two consecutive 3 SIREN layers to improve the network’s capacity. These skip- 4 connection blocks are referred to as *residual blocks*. Figure 2 5 top-right shows how the residual block is constructed. Following 6 CoordNet [4], we also apply average operations on the 7 residual block. For example, let the input of the residual block 8 be \mathbf{x} , and $f(\mathbf{x})$ be the activation after two SIREN layers. The 9 output of the residual block is $0.5(\mathbf{x} + f(\mathbf{x}))$. By multiplying 10 0.5 on the skip-connection result, the output range of one residual 11 block stays in $[-1,1]$ (which is the same as the input range) 12 instead of $[-2,2]$. This treatment can stabilize network training. 13

14 **Variable embedding.** Training each variable with a 15 separate neural network is not flexible or efficient in achieving 16 STSR for a single multivariate dataset. Ideally, we want the 17 network to support *joint training* even for different multivariate 18 datasets with various spatiotemporal resolutions while utilizing 19 their shared structural information to speed up network training. 20 By supporting joint training of multivariate datasets end-to-end 21 with one model, we can simplify the training pipeline and avoid 22 storing duplicate models for different variables. 23

24 Inspired by temporal embedding for video synthesis [26], we 25 devise *variable embedding* representing the reconstruction context 26 of different variables under the joint training scenario. It 27 embeds each variable sequence via a real-valued optimizable 28 latent vector $\Phi_{e_i} \in \mathbb{R}^l$, where l denotes the latent vector’s length. 29 When we train on the STSR task, we jointly optimize variable- 30 specific latent vectors Φ and network parameters Θ . 31

32 In Equation 1, even though all latent vectors Φ have the 33 same length of l , each e_i can have its own input coordinates 34 \mathbf{C}_{e_i} . Therefore, denoted by \mathcal{F}_Θ , the network can train variables 35 with different spatial or temporal resolutions jointly. One 36 intuitive way to encode the reconstruction task’s context information 37 for each variable is to apply *one-hot vector*. Such a 38 vector has a fixed length containing n bits of 0 and 1. For the 39 one-hot vector of e_i , only the i -th bit is 1, and the rest are 0. 40 Compared to one-hot vectors, our variable embedding offers 41 the following benefits. First, one-hot vectors are a *disentangled* 42 form of representation, but our learnable latent vectors are *distributed*. The 43 length of our latent vectors does not increase as the 44 number of variables increases. Second, one-hot vectors can 45

46 only be *orthogonal* to each other, but our learnable latent vectors 47 are updated during training to implicitly encode *differentiations* 48 among variables. Once trained, variable embedding can 49 describe the distribution difference between variables. Third, 50 variable embedding has the potential to provide an *operable* 51 latent space, where interpolating between these optimized latent 52 vectors can infer novel results with an appropriate decoder. 53

54 **Modulated structure.** Unlike CoordNet, STSR-INR needs 55 to embed variable information into different variable-specific 56 latent vectors. To this end, designing a way to condition the 57 network output with different latent vectors is necessary. An 58 intuitive way to condition learnable latent vectors on the 59 generative network is to concatenate the latent vectors with 60 coordinates as input to the INR model. Works like DeepSDF [25] 61 follow this path. However, as pointed out by Mehta et al. [28], 62 the *concatenation* approach is less expressive compared with 63 a *modulation* approach. Concatenating the latent vectors with 64 input only changes the *phase* of the feature map, while 65 modulation allows the latent vectors to control the *phase*, *frequency*, 66 and *amplitude* of the feature maps. Therefore, we present a 67 *modulated structure* that consists of a *modulator network* and a 68 *synthesis network*. The modulator network ingests the variable 69 embedding latent vector information and modulates the synthesis 70 network via dot product the activations of each block in the 71 two networks. Instead of using ReLU in the modulator network 72 [28], we utilize Sine as the non-linear function and keep 73 the same network structure for both networks. As a result, each 74 layer’s input and output ranges in the synthesis network remain 75 $[-1,1]$. This adaptation leads to fast and stable network training. 76

77 **Variational auto-decoder.** During training, we jointly 78 optimize network parameters Θ and conditioned learnable latent 79 vectors Φ . After that, the INR model can take trained Φ to 80 reconstruct variable sequences. In this case, Φ can be considered 81 dimensionality reduction resulting from a representation 82 learning process of high-dimensional multivariate data. We can 83 leverage the optimized Φ to generate new latent vectors and 84 infer results through the network or analyze the difference 85 between variable sequences. 86

87 As such, we leverage *variational auto-decoder* (VAD) [29] 88 that employs a strong regularization on variable embedding. 89 VAD brings two benefits. First, the learned latent space could 90 be more compact as it follows a standard normal distribution. 91 Second, we can use sampled unseen latent vectors to infer 92 smoother novel results due to the continuous and probabilistic 93 nature of the VAD latent space. Similar to *variational auto-* 94

1 *encoder* (VAE) [30], for variable e_i , instead of using one non-
2 random vector, we sample latent vector Φ_{e_i} through its opti-
3 mizable posterior distribution $N(\mu_{e_i}, \sigma_{e_i}^2)$. The distribution of
4 Φ_{e_i} cannot be optimized directly, so we apply the reparameteri-
5 zation trick [30]: $\Phi_{e_i} = \mu_{e_i} + \sigma_{e_i} \odot \varepsilon$, where ε is sampled from
6 $\varepsilon \sim N(0, \mathbf{I})$ and \mathbf{I} is the identity matrix. Then we can optimize
7 the distribution of Φ_{e_i} by optimizing μ_{e_i} and σ_{e_i} . However, our
8 experiment shows that the optimizable σ_{e_i} could lead to unsta-
9 ble training. Therefore, we only make μ_{e_i} learnable and set σ_{e_i}
10 close to a constant unit vector. Such an adaptation stabilizes
11 the training of VAD. We remove the random component in Φ_{e_i}
12 during inference and use μ_{e_i} to represent each variable. The
13 key motivation for sampling latent vectors during training is to
14 ensure the input latent space of the decoder is a continuous rep-
15 resentation instead of a discrete one like *auto-decoder* (AD).
16 By sampling latent vectors and optimizing their distributions in
17 the latent space, interpolated latent vectors are less likely to fall
18 out of the continuous latent space that the decoder can decode,
19 leading to a more meaningful reconstruction.

20 **Multi-head training.** INR methods consisting of only the
21 MLP structure usually suffer in the speeds of training and infer-
22 ence. This is because the model needs to iterate all the samples
23 sequentially. One way to solve this problem is to replace part
24 of the fully-connected layers in INR with several convolutional
25 layers so the network output can be a whole volume/image in-
26 stead of a single voxel/pixel. Works like NeRV [31] follow this
27 route. However, according to the experimental results in [4],
28 utilizing CNNs directly in the reconstruction task yields blurry
29 and noisy prediction results. Inspired by the *multi-head struc-*
30 *ture* proposed by Aftab et al. [32], we leverage a multi-head
31 strategy to significantly speed up the training without losing
32 much of the reconstruction ability. Specifically, we partition the
33 spatial volume into blocks of equal size and feed the network
34 with local coordinates. These coordinates can be mapped to the
35 voxel values of corresponding positions within each block. As
36 sketched in the left of Figure 2, after applying multiple heads
37 at the end of the network structure, each network's feedforward
38 pass can output all values corresponding to the same local co-
39 ordinate across all these spatial partitions. This strategy dra-
40 matically reduces the necessary floating point operations for
41 reconstructing the whole signal. Furthermore, by considering
42 the difference of volume blocks in each partition, each head
43 of our network utilizes its independent parameters to process
44 the shared features output by the modulator and synthesis net-
45 works. This treatment ensures that the network can fit the vol-
46 ume sequence efficiently. Figure 2 bottom-right shows how the
47 head part is constructed. Compared to the standard one-head
48 training, our network requires proportionally fewer feedforward
49 passes as the number of heads increases.

50 3.3. Optimization

In the training process, we jointly optimize network par-
51 ameters Θ and learnable latent vectors Φ . The objective function
52 consists of two parts: *reconstruction* loss and *Kullback-Leibler*
53 *divergence* (KLD) loss [33]. The total loss \mathcal{L} is given by

$$54 \mathcal{L} = \mathcal{L}_{\text{REC}} + \lambda \mathcal{L}_{\text{KLD}}, \quad (2)$$

55 where \mathcal{L}_{REC} and \mathcal{L}_{KLD} are the reconstruction and KLD losses,
56 and $\lambda \in [0, 1]$ controls the weight of the KLD term.

57 **Reconstruction loss.** Given the input coordinates and latent
58 vectors, the network predicts the corresponding voxel values
59 \mathbf{V}_{PRE} . Let the ground-truth voxel values be \mathbf{V}_{GT} (in our case,
60 low-resolution volumes), and the reconstruction loss is defined
61 as

$$62 \mathcal{L}_{\text{REC}} = \|\mathbf{V}_{\text{PRE}} - \mathbf{V}_{\text{GT}}\|_2. \quad (3)$$

63 **KLD loss.** Like VAE [30], we add a KLD term to regularize
64 the variable latent space and secure plausible interpolation re-
65 sults among various latent vectors. Let the prior distribution of
66 the latent vector Φ_{e_i} be $q(\Phi_{e_i} | \mathbf{D}_{e_i})$. The KLD term is defined as

$$67 \mathcal{L}_{\text{KLD}} = \sum_{i=1}^n \text{KLD}(q(\Phi_{e_i} | \mathbf{D}_{e_i}) || p(\mathbf{D}_{e_i} | \Phi_{e_i})). \quad (4)$$

68 In the following experiment, we set our prior distribution
69 $q(\Phi_{e_i} | \mathbf{D}_{e_i})$ as the Gaussian distribution where $p(\mathbf{D}_{e_i} | \Phi_{e_i})$ is the
70 distribution of sampled latent vector. Therefore, the expanded
71 form of Equation 4 then becomes

$$72 \mathcal{L}_{\text{KLD}} = \frac{1}{2} \sum_{i=1}^n (\sigma_{e_i}^2 + \mu_{e_i}^2 - 1 - \log \sigma_{e_i}^2). \quad (5)$$

73 For stable training, we do not optimize σ_{e_i} and only update μ_{e_i} .
74 The value of μ_{e_i} is randomly initialized and the constant value of
75 $\sigma_{e_i}^2$ is set by making $\log \sigma_{e_i}^2 = 10^{-3}$. As such, the effect of the
76 KLD loss is to regulate the different latent vector distributions
77 to be close in the latent space. This ensures that the interpolated
78 latent vector among them is less likely to fall outside the mean-
79 ingful latent space region the decoder can decode. However, the
80 decoder may suffer in the optimization process when different
81 distributions are too close. Therefore, we introduce λ in Equa-
82 tion 2 to control the strength of KLD regulation. Algorithm 1
83 outlines the STSR-INR training process.

Algorithm 1 STSR-INR training algorithm

84 **Input:** Dataset $\mathbf{D} = \{(\mathbf{C}_{e_i}, \mathbf{V}_{e_i})\}_{i=1}^n$, target training
85 epochs T , distribution variances of latent vectors
86 $\sigma^2 = \{\sigma_{e_1}^2, \sigma_{e_2}^2, \dots, \sigma_{e_n}^2\}$, KLD loss weight λ
87 Randomly initialize network parameters Θ and distribution
88 means of latent vectors $\mu = \{\mu_{e_1}, \mu_{e_2}, \dots, \mu_{e_n}\}$
89 **for** $j = 1 \dots T$ **do**
90 **for all** $(\mathbf{C}_{e_i}, \mathbf{V}_{e_i}) \in \mathbf{D}$ **do**
91 $\Phi_{e_i} \leftarrow \mu_{e_i} + \sigma_{e_i} \odot \varepsilon$, where $\varepsilon \sim N(0, \mathbf{I})$
92 Calculate $\mathbf{V}_{\text{PRE}} \leftarrow \mathcal{F}_{\Theta}(\mathbf{C}_{e_i}; \Phi_{e_i})$
93 Compute \mathcal{L}_{REC} following Equation (3)
94 Update (Θ, μ) based on \mathcal{L}_{REC}
95 **end for**
96 Compute \mathcal{L}_{KLD} following Equation (5)
97 Update μ based on $\lambda \mathcal{L}_{\text{KLD}}$
98 **end for**

4. Results and Discussion

64 4.1. Datasets and Network Training

65 **Datasets.** Table 1 lists the datasets used in our exper-
66 iments. The variable set of the combustion dataset [34] includes

51
5253
54
55
56
57
58
59
60
61
62
6364
65
66
67

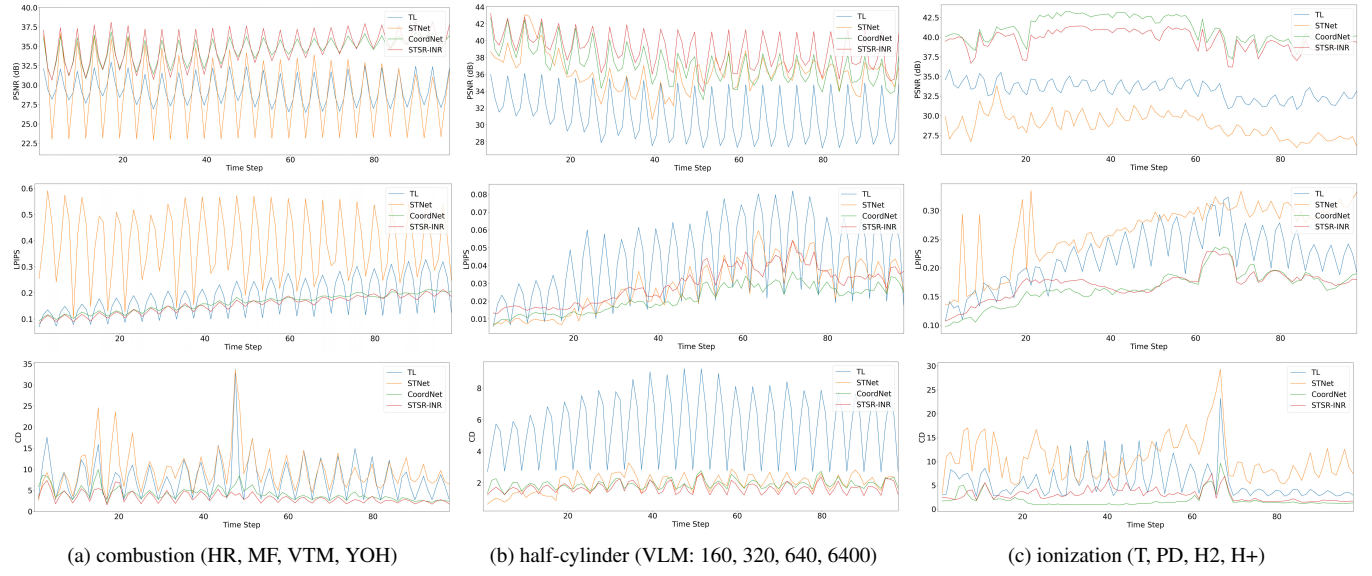


Fig. 3: Average PSNR (dB, top row), LPIPS (middle row), and CD (bottom row) values over the experimented variables of the three datasets.

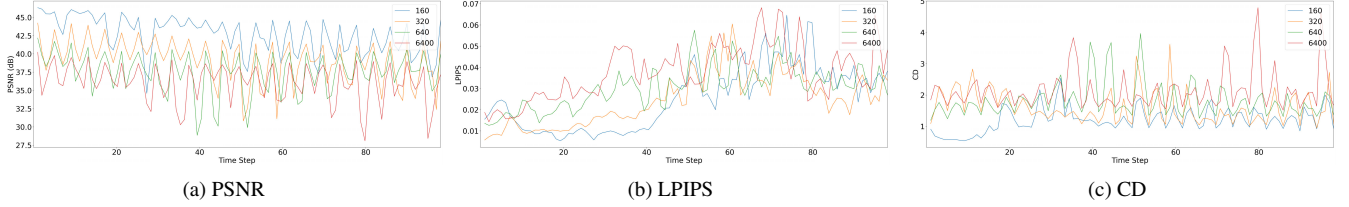


Fig. 4: PSNR (dB), LPIPS, and CD values for individual ensemble members of the half-cylinder (VLM) dataset using STSR-INR.

heat release (HR), mixture fraction (MF), vorticity magnitude (VTM), and OH mass fraction (YOH). The half-cylinder ensemble dataset [35] was produced from a fluid simulation under different Reynolds numbers (160, 320, 640, 6400). We use velocity magnitude (VLM). The ionization dataset [36] was produced from 3D radiation hydrodynamical calculations of the ionization front instabilities, and we use five variables: gas temperature (T), total particle density (PD), and mass abundances of H+, H2, and He. The Tangaroa dataset [37] has four variables: acceleration (ACC), divergence (DIV), VLM, and VTM. Finally, we also use three single-variable datasets: five-jet, tornado, and vortex, for additional experiments. Their variables are energy (E), VLM, and VTM.

Network training. The training and inference were performed on a single NVIDIA Tesla P100 graphics card with 16 GB of memory. The input spatial and temporal coordinates and target volume values were normalized to $[-1, 1]$. The modulator network and synthesis network both have five residual blocks. We leverage 8-head in our network structure to achieve a trade-off between quality and speed (refers to Section 4.5). The network parameters were initialized following Sitzmann et al. [18]. Note that when applying the multi-head strategy to our STSR-INR model, we set the hyperparameter $\omega_0 = 5$ according to Yüce et al. [38]. This is to avoid utilizing aliased higher-frequency components for volume reconstruction with a low-sampling frequency. We set the batch size as 8000 total sampling points across all variables. We used Adam with a learning rate of 10^{-5} , $\beta_1 = 0.9$, $\beta_2 = 0.999$, and L_2 weight

decay of 10^{-6} . The weight of KLD loss λ was set to 10^{-3} . We trained STSR-INR for 600 epochs to converge.

Table 1: Variables and resolution of each dataset.

dataset	variables or ensembles	resolution ($x \times y \times z \times t$)
combustion [34]	HR, MF, VTM, YOH	$480 \times 720 \times 120 \times 100$
half-cylinder [35]	VLM: 160, 320, 640, 6400	$640 \times 240 \times 80 \times 100$
ionization [36]	T, PD, H+, H2, He	$600 \times 248 \times 248 \times 100$
Tangaroa [37]	ACC, DIV, VLM, VTM	$300 \times 180 \times 120 \times 150$
five-jet	E	$128 \times 128 \times 128 \times 2000$
tornado [39]	VLM	$128 \times 128 \times 128 \times 48$
vortex [40]	VTM	$128 \times 128 \times 128 \times 90$

Table 2: Average PSNR (dB), LPIPS, and CD values for training across multiple variables and all timesteps. We list the experimented variables and chosen isovales for computing CD. $u_s = 4$ and $u_t = 3$. The best quality performances are shown in bold.

dataset	method	PSNR \uparrow	LPIPS \downarrow	CD \downarrow
combustion (HR, MF, VTM, YOH) ($v = 0.3, 0.0, 0.0, 0.0$)	TL	29.10	0.195	7.81
	STNet	28.97	0.387	9.65
	CoordNet	34.43	0.165	4.20
	STSR-INR	34.68	0.158	3.42
half-cylinder (VLM: 160, 320, 640, 6400) ($v = 0.0, 0.0, 0.0, 0.0$)	TL	30.79	0.043	5.68
	STNet	36.19	0.028	1.98
	CoordNet	36.87	0.022	2.02
	STSR-INR	38.59	0.029	1.77
ionization (T, PD, H2, H+) ($v = 0.0, 0.0, -0.7, -0.3$)	TL	33.16	0.224	5.76
	STNet	29.72	0.264	10.63
	CoordNet	40.85	0.167	1.87
	STSR-INR	39.62	0.172	3.00

4.2. Baselines and Evaluation Metrics

Baselines. We compare our STSR-INR with three baseline solutions:

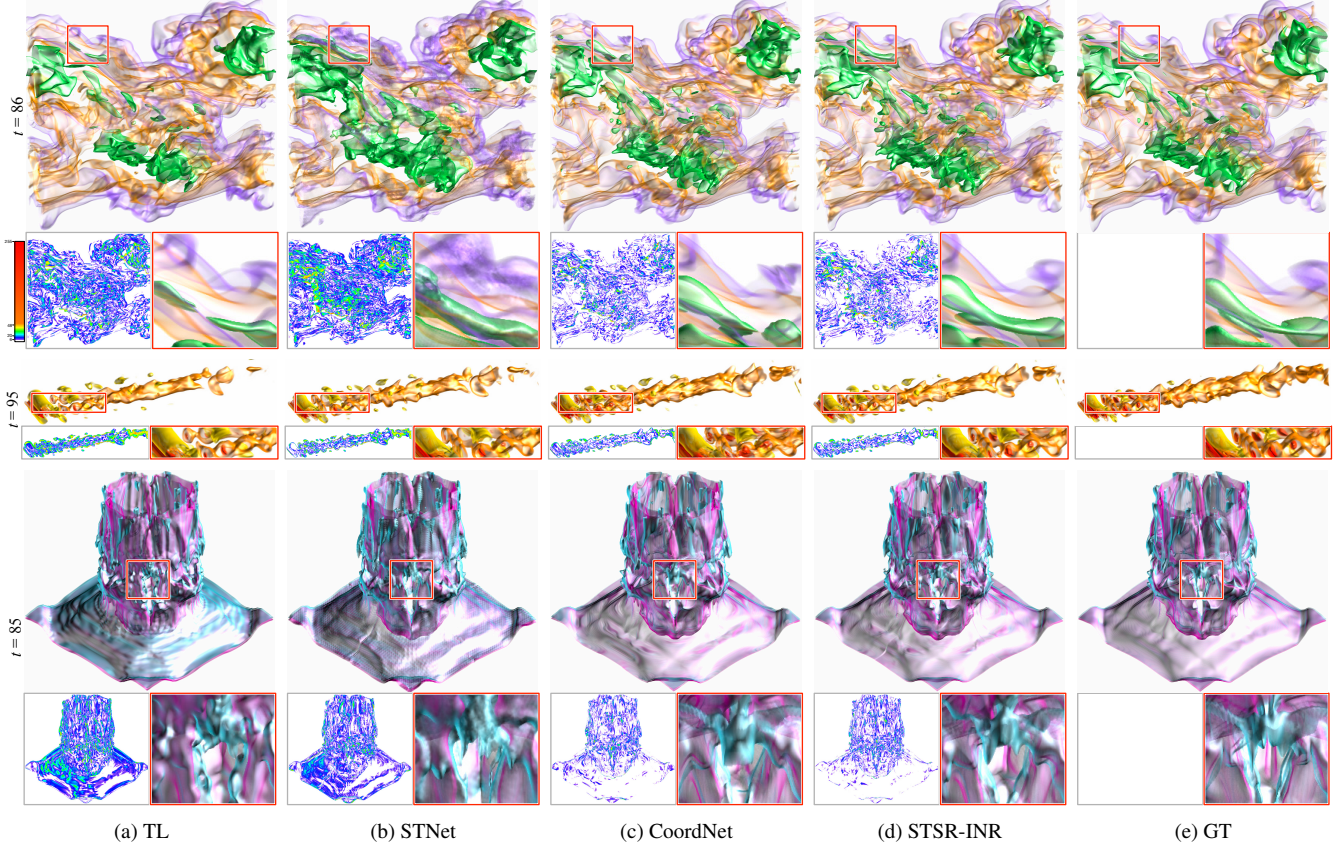


Fig. 5: Super-resolution: comparing volume rendering results. Top to bottom: combustion (YOH), half-cylinder (VLM: 320), and ionization (H+).

Table 3: Total training and inference time (hours) and the model size (MB) for the ionization (T, PD, H2, H+) dataset. $u_s = 4$ and $u_t = 3$.

method	training	inference	model
STNet	25.9	1.5	62.56
CoordNet	19.6	5.5	5.67
STSR-INR	22.9	3.7	5.41

1 • TL applies tricubic interpolation on the spatial domain,
2 followed by linear interpolation on the temporal domain to
3 upscale volumes in space and time, respectively, to achieve
4 STSR.

5 • STNet [2] is an end-to-end GAN-based STSR model. We
6 train one STNet on all variables to handle multivariate
7 datasets simultaneously to achieve multivariate STSR
8 learning. The network structure of STNet remains the
9 same, and it does not differentiate variables. We treat
10 volumes of different variables as additional samples for training
11 and inference.

12 • CoordNet [4] is a general INR network for data generation
13 and visualization generation tasks. For STSR, the network
14 takes spatiotemporal coordinates as input and outputs cor-
15 responding voxel values. We modify CoordNet by chang-
16 ing the last output layer from inferring the voxel value of
17 one variable to those of multiple variables.

18 The training epochs for STNet (including pre-training and
19 fine-tuning) and CoordNet follow the suggestions given in Han
20 et al. [2] and Han and Wang [4], and we empirically found
21 those hyperparameter work well on most datasets. Note that

22 STNet can only upscale the input dataset with fixed spatial and
23 temporal upscale factors (u_s and u_t). It requires low- and high-
24 resolution volume pairs for supervised training. In contrast, Co-
25 ordNet and STSR-INR support arbitrary u_s and u_t , and they can
26 train the network in an unsupervised manner. However, when
27 training on STSR tasks for multivariate or ensemble datasets,
28 CoordNet can only work with multiple datasets of the same spa-
29 tiotemporal resolution in the same network. Unlike CoordNet,
30 STSR-INR can train and infer multiple multivariate datasets of
31 different spatiotemporal resolutions in the same network.

32 **Evaluation metrics.** We evaluate our reconstruction results
33 based on three metrics. We utilize *peak signal-to-noise ratio*
34 (PSNR) at the data level, *learned perceptual image patch*
35 *similarity* (LPIPS) [41] at the image level, and *chamfer distance*
36 (CD) [42] at the surface level. The calculation is based
37 on the data, volume rendering images, and isosurfaces coming
38 from the original data and their corresponding version gener-
39 ated from one of the methods.

4.3. Results

41 **Quantitative results.** Table 2 reports the quantitative results
42 of the four methods across three metrics over three datasets,
43 given the spatial and temporal upscale factors of 4 and 3. STNet
44 performs the worst for the combustion dataset, followed by TL
45 and CoordNet. STSR-INR achieves the best results. TL per-
46 forms the worst for the half-cylinder (VLM) dataset, while the
47 other three methods get similar results, with STSR-INR yield-
48 ing the best results for PSNR and CD values. STNet gets the

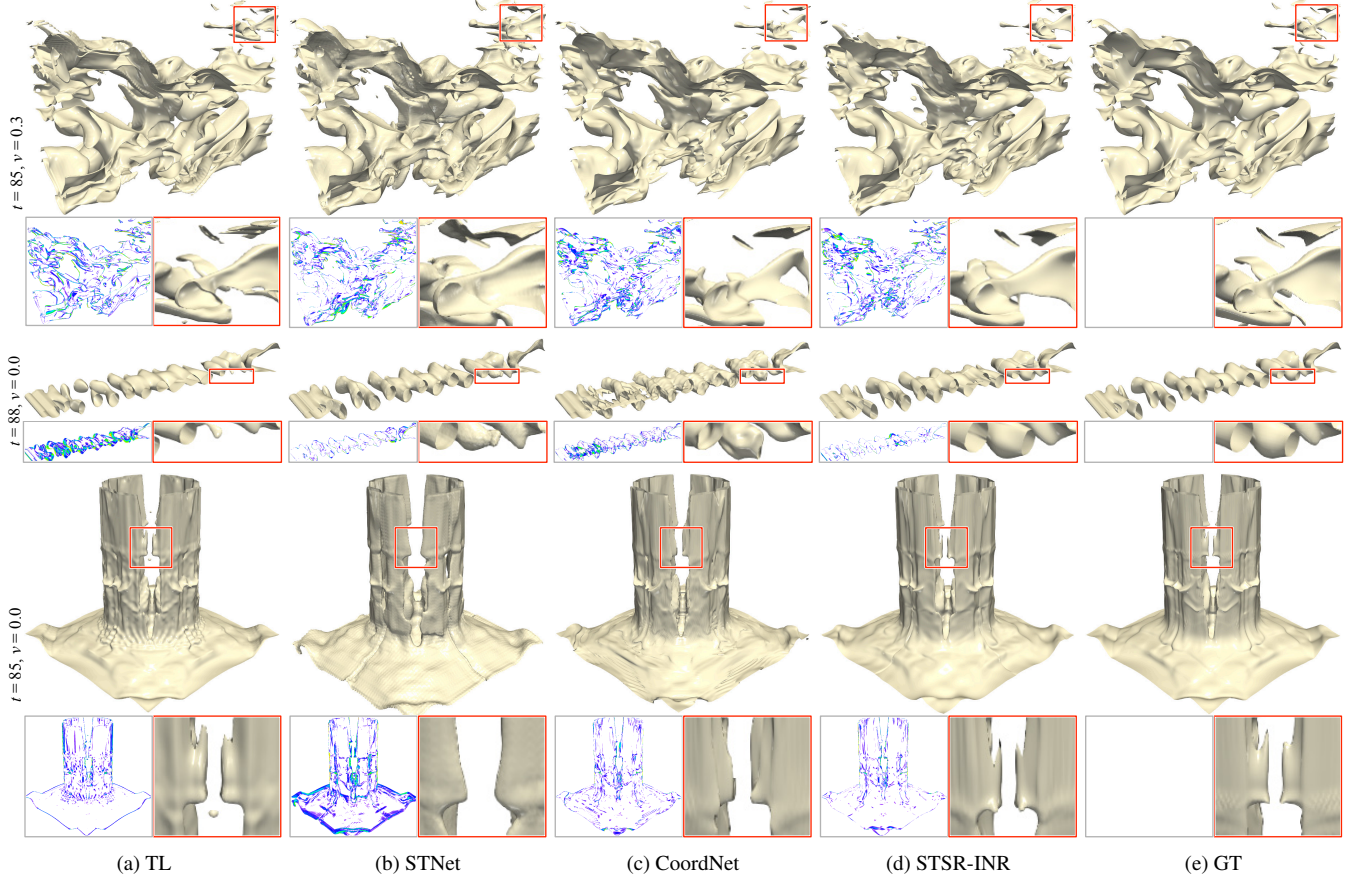


Fig. 6: Super-resolution: comparing isosurface rendering results. Top to bottom: combustion (HR), half-cylinder (VLM: 160), and ionization (T).

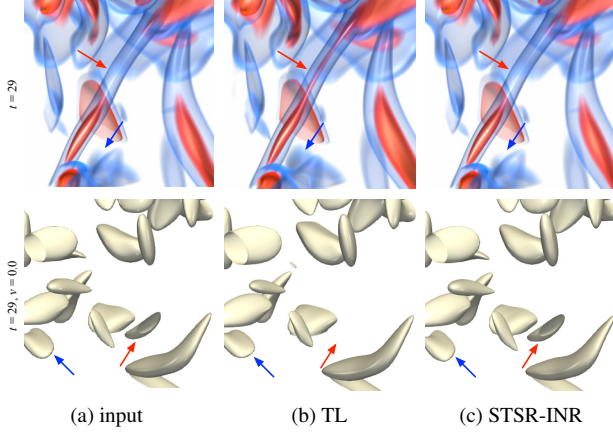


Fig. 7: Unsupervised training: comparing volume rendering and isosurface rendering of the vortex dataset. $u_s = 1.75$ and $u_t = 2.5$.

worst results for the ionization dataset, followed by TL. CoordNet outperforms STSR-INR. Overall, we can summarize that CoordNet and STSR-INR are the two top methods among these four, and STSR-INR has a slight edge over CoordNet, considering the parameters size of STSR-INR is slightly smaller than CoordNet (as described in Table 3). We attribute STNet's inferior performance to the simultaneous training of multiple variables with various structural appearances, which negatively impacts the discernibility of its temporal discriminator. On the

other hand, the interpolation of TL only leverages local neighboring voxel values instead of the global pattern, which leads to a less accurate reconstruction.

In Figure 3, we plot the three metrics over time averaged across the variables for these three datasets. The periodical rises and falls on each performance curve are due to the setting of temporal upscale factor $u_t = 3$. The timesteps used for training are $\{1, 5, 9, \dots\}$ (high performance) and the synthesized ones are $\{2, 3, 4, 6, 7, 8, \dots\}$ (low performance). In Figure 4, we plot the three metrics for each ensemble of the half-cylinder (VLM) dataset. As expected, the higher the Reynolds number, the more turbulent or complex the underlying flow, and the worse the performance.

Qualitative results. Figure 5 shows volume rendering results generated from data produced by these four methods and GT data using combustion (YOH), half-cylinder (VLM: 320), and ionization (T) datasets. To pinpoint the differences, we compute the pixel-wise difference images (i.e., the Euclidean distance in the CIELUV color space) between each method and GT. Noticeable differences are mapped to purple, blue, green, yellow, and red, showing low to high pixel-wise differences (refer to the top-left image of Figure 5 for the colormap legend). In addition, we also highlight a zoom-in region for a closer comparison. These visual comparison results confirm that CoordNet and STSR-INR are better than TL and STNet. Between CoordNet and STSR-INR, STSR-INR leads to rendering results closer to GT renderings.

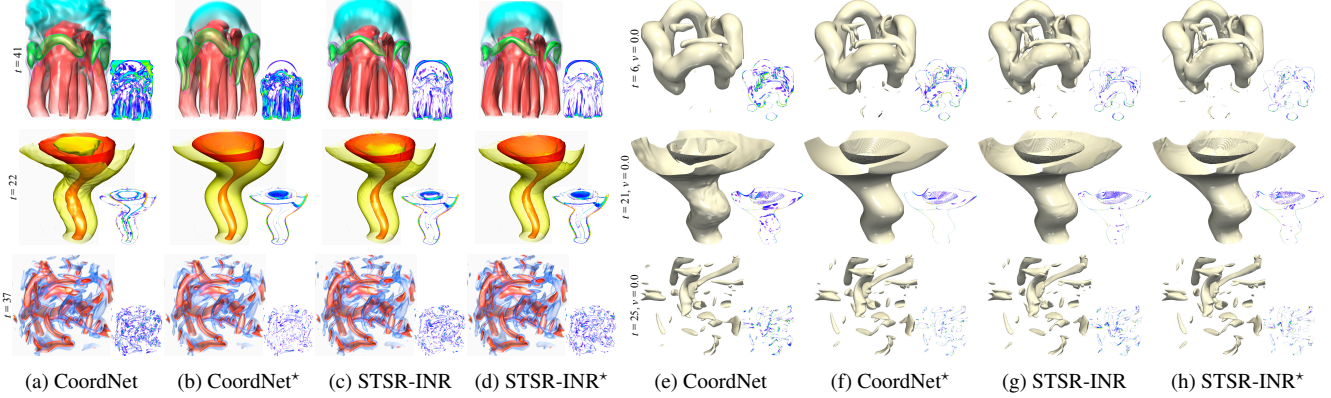


Fig. 8: Joint training of datasets with the same resolution: comparing volume rendering and isosurface rendering results for the same spatial and temporal upscale factors. Top to bottom: five-jet, tornado, and vortex. CoordNet* and STSR-INR* denote separate training.

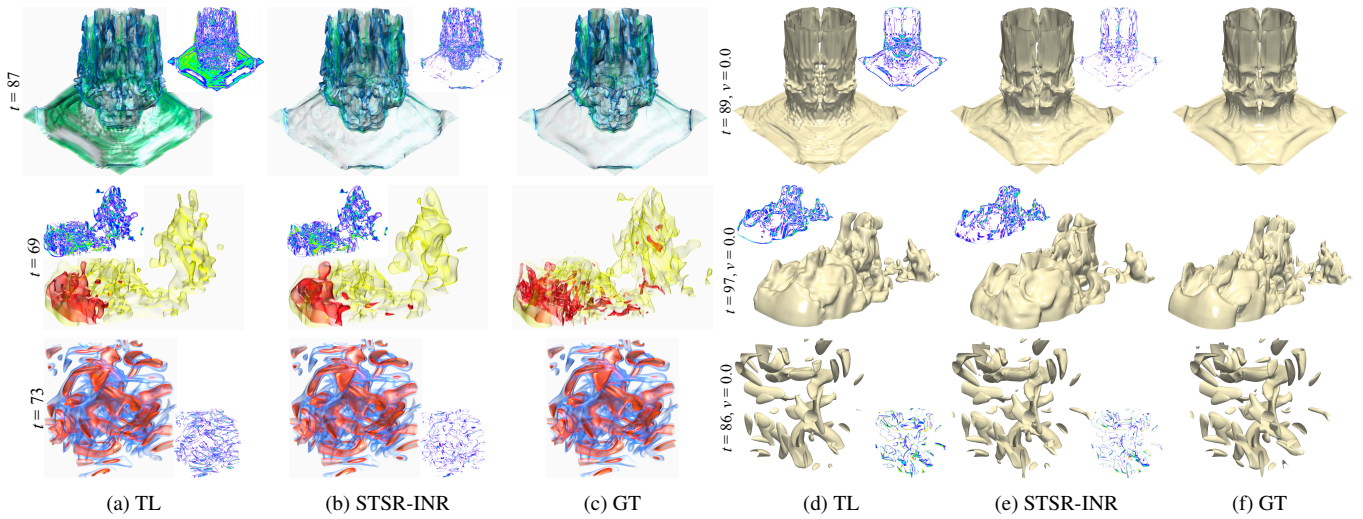


Fig. 9: Joint training of datasets with different resolutions: comparing volume rendering and isosurface rendering results for different spatial and temporal upscale factors. Top to bottom: ionization (He), Tangaroa (VLM), and vortex.

In Figure 6, we show isosurface rendering results generated from these methods using the same datasets as Figure 5 but with different variables. Although the difference images reveal more subtle rendering deviations from GT, the zoom-in regions all indicate that STSR-INR yields isosurfaces most similar to GT while keeping the overall rendering image difference small. CoordNet leads to non-smooth surfaces with clear visual artifacts for the half-cylinder (VLM: 160) dataset. The same can be observed for TL and STNet of the combustion (HR) dataset and TL and CoordNet of the ionization (T) dataset.

Timing and model size. In Table 3, we report the training and inference time of the STSR task and the model size on the ionization dataset for the three deep learning methods: STNet, CoordNet, and STSR-INR. In terms of training, CoordNet achieves the fastest convergence speed. On the other hand, due to the use of multi-head training, STSR-INR takes more time to approximate its optimal parameters for each head (refer to Section 4.5 for an additional performance tradeoff study of STSR-INR with different head settings). STNet requires the most training time because of its larger model size and complicated training pipeline. For inference, the CNN- and LSTM-based STNet requires the shortest time. STSR-INR achieves a

faster inference speed than CoordNet as the multi-head structure enables the model to effectively decrease the number of necessary feedforward passes to reconstruct the whole dataset. As for the mode size, STNet has the largest size due to its CNN network structure. CoordNet and STSR-INR have an order of magnitude smaller model size thanks to their MLP structure.

4.4. Unsupervised Training and Joint Training

Unsupervised training. The INR-based solutions allow us to perform unsupervised spatiotemporal super-resolution training where the trained resolution is at the original resolution. We aim to upscale the data to higher-resolution ones with no GT data available for training and comparison. To evaluate unsupervised training of STSR-INR, we compare TL and STSR-INR using the vortex dataset. To demonstrate that STSR-INR permits data upscaling with arbitrary scale factors, we use non-integer upscale factors $u_s = 1.75$ and $u_t = 2.5$, upscaling the original resolution from $128 \times 128 \times 128 \times 90$ to $224 \times 224 \times 224 \times 225$.

Figure 7 shows the zoomed-in volume rendering and isosurface rendering results. The input low-resolution reveals the jaggy surface boundary in the isosurface rendering. TL and

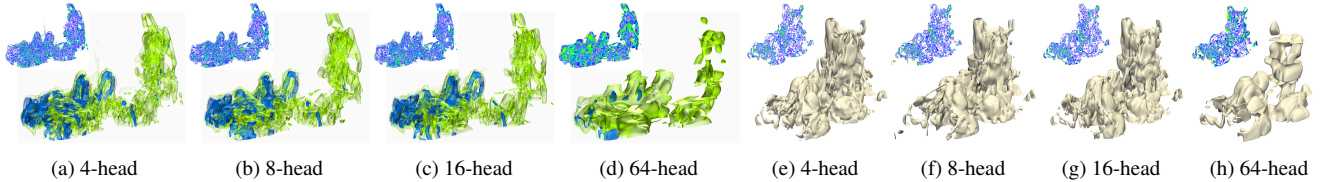


Fig. 10: Multi-head training: comparing volume rendering (VTM, $t = 74$) and isosurface rendering (ACC, $t = 61$, $v = -0.7$) of the Tangaroa dataset.

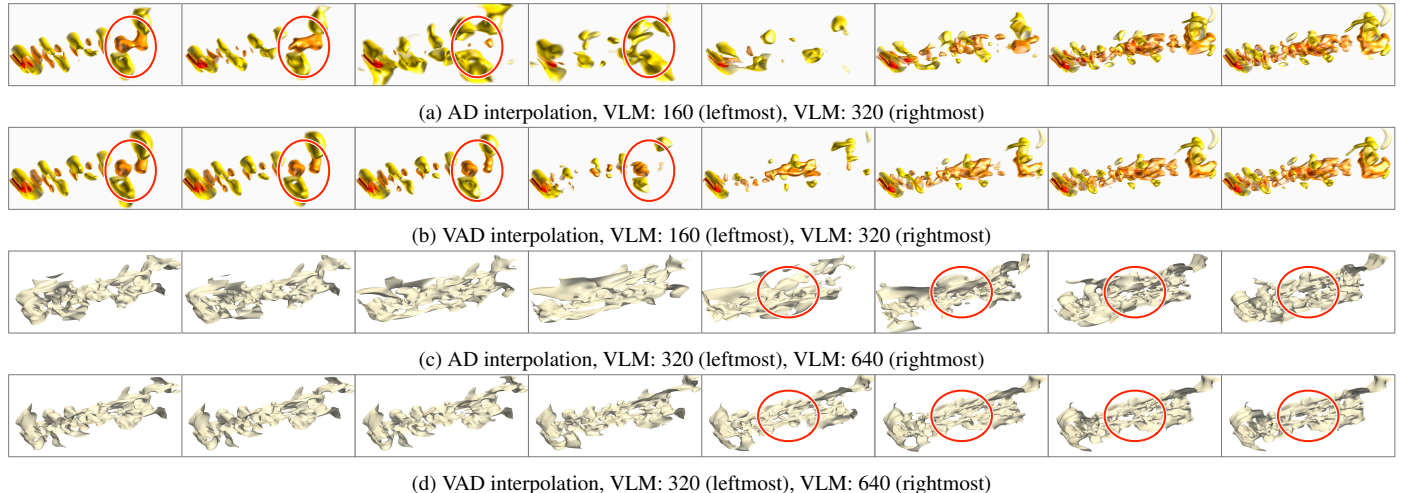


Fig. 11: Latent-space interpolation: comparing volume rendering and isosurface rendering of the half-cylinder (VLM) dataset. $t = 49$ and $v = 0.3$.

Table 4: Average PSNR (dB), LPIPS, and CD values for joint training datasets of the same (top part) and different (bottom part) resolutions. CoordNet* and STSR-INR* denote separate training (only the better ones of CoordNet and STSR-INR are bolded).

dataset	method	PSNR \uparrow	LPIPS \downarrow	CD \downarrow
five-jet	CoordNet	36.84	0.181	2.65
$(u_s = 2, u_t = 3, v = 0.0)$	CoordNet*	38.46	0.140	1.51
	STSR-INR	39.33	0.103	1.08
	STSR-INR*	39.72	0.079	0.99
tornado	CoordNet	37.19	—	—
$(u_s = 2, u_t = 3, v = 0.0)$	CoordNet*	39.05	0.076	0.68
	STSR-INR	40.19	0.091	0.54
	STSR-INR*	39.75	0.092	0.71
vortex	CoordNet	31.96	—	—
$(u_s = 2, u_t = 3, v = 0.0)$	CoordNet*	37.25	0.065	0.87
	STSR-INR	35.25	0.076	1.04
	STSR-INR*	37.06	0.070	0.89
ionization (He)	TL	25.27	0.195	3.03
$(u_s = 4, u_t = 5, v = 0.0)$	STSR-INR	33.40	0.113	0.97
Tangaroa (VLM)	TL	29.29	—	—
$(u_s = 5, u_t = 7, v = 0.0)$	STSR-INR	32.23	0.129	2.89
vortex	TL	30.16	—	—
$(u_s = 2, u_t = 3, v = 0.0)$	STSR-INR	37.17	0.064	0.79

1 STSR-INR give smooth boundaries. However, as the arrows
2 indicate, the super-resolution results of STSR-INR are closer to
3 input than TL. TL introduces non-existing artifacts (red arrows
4 in the volume rendering images) or misses a surface component
5 (red arrows in the isosurface rendering images) due to its lack
6 of ability to extract the global pattern from low-resolution data.
7 This demonstrates the advantage of STSR-INR over straight-
8 forward TL.

9 **Joint training of datasets with the same resolution.** Due
10 to their network differences, in each training epoch, CoordNet
11 “sees” all the variables’ values at a specific spatiotemporal co-
12 ordinate while we only allow STSR-INR to update the par-
13 ameters of one variable. Therefore, CoordNet fits datasets where

Table 5: Average PSNR (dB), LPIPS, CD values, model sizes (MB), training time (hours), and speed-ups with STSR-INR for the Tangaroa (ACC, DIV, VLM, VTM) dataset. $u_s = 4$, $u_t = 3$, and $v = (-0.7, -0.9, 0.1, -0.8)$. A similar GPU memory size is used for all these cases during training.

# heads	PSNR \uparrow	LPIPS \downarrow	CD \downarrow	model	training	speed-up
1	35.91	0.124	2.31	5.41	43.75	1×
4	35.55	0.129	2.70	5.41	9.83	4.5×
8	35.56	0.128	2.55	5.41	5.95	7.4×
16	35.58	0.132	2.68	5.41	4.42	9.9×
64	33.11	0.187	5.90	5.41	3.38	12.9×
512	30.29	0.302	15.53	5.53	13.25	3.3×

Table 6: Average PSNR (dB), LPIPS, and CD values with STSR-INR for the half-cylinder (VLM: 160, 320, 640, 6400) dataset. $u_s = 4$, $u_t = 3$, and $v = 0.3$.

scheme	PSNR \uparrow	LPIPS \downarrow	CD \downarrow
AD	38.02	0.022	5.67
VAD	38.59	0.029	6.59

14 the variables share similar appearances better than STSR-INR
15 because CoordNet spends less effort identifying the relationship
16 between different variables (refer to the performance re-
17 sults of the ionization dataset shown in Table 2). However, the
18 performance could drop when tackling datasets where the vari-
19 ables exhibit diverse appearances. Still, STSR-INR is robust in
20 handling this scenario. Here, we conduct a comparative study
21 on three variables from different datasets (five-jet, tornado, and
22 vortex), and these variables have no relationship. Each variable
23 has a spatial resolution of $128 \times 128 \times 128$. Because CoordNet
24 can only train and infer on datasets with the same spatiotem-
25 poral resolution, we select a subset of timesteps for five-jet and
26 vortex datasets to match the temporal resolution (48 timesteps)
27 of the tornado dataset.

As shown in the top part of Table 4, between CoordNet and
28 STSR-INR, STSR-INR is the winner of eight out of nine met-

rics across the three variables from different datasets. To better demonstrate the performance drop of CoordNet, we evaluate the performance of separate training for both CoordNet and STSR-INR, denoted as CoordNet* and STSR-INR*. Compared with joint training, STSR-INR and STSR-INR* have a small performance gap for the five-jet and tornado datasets and a drop of 1.81dB in PSNR for the vortex dataset. However, CoordNet suffers a large drop for all three datasets, especially for the vortex dataset, where a drop of 5.29dB in PSNR is reported. Figure 8 shows the rendering results. For volume rendering, STSR-INR yields closer results than CoordNet for five-jet and vortex, only losing to CoordNet at the top region of the tornado while better preserving the overall shape. For isosurface rendering, STSR-INR beats CoordNet for all three datasets. Between STSR-INR and STSR-INR*, STSR-INR produces results of better quality for tornado (volume rendering and isosurface rendering), slightly worse quality for five-jet (isosurface rendering) and vortex (volume rendering and isosurface rendering), and worse quality for five-jet (volume rendering). Again, the visual differences are marginal in all cases. For all three datasets, the visual quality of CoordNet is inferior to that of CoordNet*. By comparing the performance differences between CoordNet and CoordNet*, as well as STSR-INR and STSR-INR*, we observe robust reconstruction of STSR-INR even though the variables exhibit diverse differences. This also suggests that joint training for STSR-INR only incurs slight performance drops, which makes it a feasible alternative to separate training.

Joint training of datasets with different resolutions. Unlike CoordNet and STNet, a significant advantage of STSR-INR is that it permits joint training across multivariate datasets with different spatiotemporal resolutions and upscale factors. We use ionization (He), Tangaroa (VLM), and vortex datasets with varying u_s and u_t to evaluate the joint-training performance of STSR-INR. For network training, the input spatiotemporal resolutions of these datasets are $150 \times 62 \times 62 \times 17$, $60 \times 36 \times 24 \times 19$, and $64 \times 64 \times 64 \times 23$, respectively.

The bottom part of Table 4 shows that STSR-INR beats TL for eight out of nine metrics across the three variables from different datasets. Figure 9 gives the rendering results. For volume rendering, STSR-INR beats TL for ionization (He) and vortex and falls behind TL slightly for Tangaroa (VLM). For isosurface rendering, STSR-INR leads to closer results than TL for ionization (He) and vortex and produces isosurfaces of similar quality for Tangaroa (VLM), while the average CD over all timesteps is still better than TL.

4.5. Network Analysis

To analyze STSR-INR, we conduct network analysis on two key settings: multi-head and VAD. In the appendix, we study the impact of network depth, latent vector length, and ReLU vs. Sine modulator activation function on network performance.

Multi-head analysis. The multi-head design serves as a speed-up option for STSR-INR. However, when implementing this scheme, we need to concatenate the output of different heads to produce the reconstruction results, which could impact the downstream rendering quality. Here, we use the Tangaroa dataset to evaluate the relationship of head numbers with reconstruction quality, model size, and speed-up. We experiment

with five head settings (4, 8, 16, 64, and 512). For 8-head, 64-head, and 512-head, we partition the volume along the x , y , and z axes once, twice, and thrice, respectively. For 4-head, we only partition along the x and y axes once, as the z dimension has the lowest resolution. For 16-head, we further partition along the x axis once based on the 8-head partition result because the x dimension has the highest resolution.

Table 5 reports the quantitative results. We observe that the speed-up of STSR-INR does not always increase linearly as the number of increases. The increasing head-branching structure incurs additional memory access costs for each head's output. When the number of heads increases to a large number (64 or 512), the memory access costs can be rather high, which leads to a decline in the speed-up performance. Figure 10 shows the rendering results for selective cases. The difference images are with respect to the 1-head rendering results. The quality remains similar for volume rendering and isosurface rendering with 4-, 8-, and 16-head settings. With 64-head, the results deteriorate tremendously. For quality, speed, and generalization tradeoffs, we recommend the 8-head setting for STSR-INR, and all results for STSR-INR reported in this paper use this setting.

VAD analysis. To validate the effectiveness of VAD, we train the half-cylinder (VLM) dataset with and without using VAD. For the model without VAD, STSR-INR simply uses an AD to optimize the variable-specific latent vectors Φ that are randomly initialized, and there is no sampling process and KLD loss computation. Thus, the training gets easier. After training, we interpolate the optimized latent vectors to produce intermediate volumes.

Even though Table 6 shows that metric-wise, AD and VAD have slight differences, the VAD-interpolated results lead to smoother and more realistic intermediate renderings than those obtained using AD, as shown in Figure 11. Note that the renderings displayed at both ends of the figure are not identical due to the model's use of AD or VAD. The highlighted ellipses indicate that VAD captures the evolution of volumetric and surface components, while AD yields inconsistent interpolation results. This analysis suggests that compared with AD, the training pipeline of VAD preserves more meaningful "semantic" information about the encoded variables. Note that our latent-space interpolation is different from the surrogate model [43, 44] that takes simulation parameters as input. Latent-space interpolation implicitly models the relationship among different variables, which is less powerful and cannot be treated as a replacement for a surrogate model.

4.6. Limitations

Even though STSR-INR can efficiently reconstruct spatiotemporally-resolved multivariate volume sequences with good quality and support latent-space interpolation, it still faces several limitations. First, STSR-INR can utilize a multi-head strategy to speed up the training and inference process, but its inference speed is still slower than the CNN-based STNet method (refer to Table 3). Meanwhile, the multi-head strategy lacks scalability due to the performance drop as the number of heads increases (refer to Table 5). Second, when different variables in the dataset share similar appearances,

1 STSR-INR could struggle to identify the value relationships
 2 among them, leading to a lower reconstruction accuracy than
 3 CoordNet (refer to the ionization case in Table 2). Third,
 4 for datasets with subtle temporal fluctuation (e.g., five-jet),
 5 STSR-INR might not capture such temporal variation when u_t
 6 is large or happens to match the fluctuation frequency (refer to
 7 the accompanying video showing joint training of datasets with
 8 the same resolution). We observe this regardless of whether
 9 joint training or separate training is employed. Fourth, like
 10 CoordNet, STSR-INR performs training and inference on the
 11 normalized data and, therefore, cannot recover the data to its
 12 original range. This might impede domain scientists' data
 13 examination in certain specialized use cases.

14 5. Conclusions and Future Work

15 We have presented STSR-INR, a new deep-learning solution
 16 for generating simultaneous spatiotemporal super-resolution for
 17 multivariate time-varying datasets. Using VAD and a modu-
 18 lated structure, STSR-INR focuses on the variable dimension
 19 and supports joint training of variables from datasets with the
 20 same or even different spatiotemporal resolutions and upscale
 21 factors. This sets STSR-INR apart from state-of-the-art deep
 22 learning methods (STNet and CoordNet). We also leverage a
 23 multi-head training strategy to significantly boost the training
 24 and inference speed of STSR-INR with only a slight down-
 25 grade in quality performance. The experimental results show
 26 the advantages of STSR-INR over conventional and existing
 27 deep-learning-based solutions: it not only achieves the over-
 28 all best quality performance but also offers the most flexibility
 29 regarding arbitrary upscaling, joint training, and unsupervised
 30 training.

31 For future work, we would like to further explore the latent-
 32 space interpolation. The VAD analysis reported in Section 4.5
 33 indicates the promise of our solution in synthesizing simulation
 34 data from unseen ensemble members. We will verify this with
 35 ensemble simulation applications. Moreover, STSR-INR en-
 36 codes variable information into latent vectors. We can leverage
 37 the learned latent vectors to interpret the relationship between
 38 different variables. Finally, our current solution only trains one
 39 network from scratch at once. Domain scientists usually gen-
 40 erate new simulation outputs based on past ones. Thus, it can
 41 be efficient if the training on the newly added data can be per-
 42 formed on a previously-trained neural network incrementally.

43 Acknowledgements

44 This research was supported in part by the U.S. National
 45 Science Foundation through grants IIS-1955395, IIS-2101696,
 46 OAC-2104158, and the U.S. Department of Energy through
 47 grant DE-SC0023145. The authors would like to thank the
 48 anonymous reviewers for their insightful comments.

49 References

- [1] Wang, C, Han, J. DL4SciVis: A state-of-the-art survey on deep learning for scientific visualization. *IEEE Transactions on Visualization and Computer Graphics* 2023;29(8):3714–3733.
- [2] Han, J, Zheng, H, Chen, DZ, Wang, C. STNet: An end-to-end generative framework for synthesizing spatiotemporal super-resolution volumes. *IEEE Transactions on Visualization and Computer Graphics* 2022;28(1):270–280.
- [3] An, Y, Shen, HW, Shan, G, Li, G, Liu, J. STSRNet: Deep joint space-time super-resolution for vector field visualization. *IEEE Computer Graphics and Applications* 2021;41(6):122–132.
- [4] Han, J, Wang, C. CoordNet: Data generation and visualization generation for time-varying volumes via a coordinate-based neural network. *IEEE Transactions on Visualization and Computer Graphics* 2023;29(12):4951–4963.
- [5] Zhou, Z, Hou, Y, Wang, Q, Chen, G, Lu, J, Tao, Y, et al. Volume upscaling with convolutional neural networks. In: *Proceedings of Computer Graphics International*. 2017, p. 38:1–38:6.
- [6] Han, J, Wang, C. SSR-TVD: Spatial super-resolution for time-varying data analysis and visualization. *IEEE Transactions on Visualization and Computer Graphics* 2022;28(6):2445–2456.
- [7] Gu, P, Han, J, Chen, DZ, Wang, C. Reconstructing unsteady flow data from representative streamlines via diffusion and deep learning based denoising. *IEEE Computer Graphics and Applications* 2021;41(6):111–121.
- [8] Han, J, Zheng, H, Xing, Y, Chen, DZ, Wang, C. V2V: A deep learning approach to variable-to-variable selection and translation for multivariate time-varying data. *IEEE Transactions on Visualization and Computer Graphics* 2021;27(2):1290–1300.
- [9] Gu, P, Han, J, Chen, DZ, Wang, C. Scalar2Vec: Translating scalar fields to vector fields via deep learning. In: *Proceedings of IEEE Pacific Visualization Symposium*. 2022, p. 31–40.
- [10] Jiao, C, Bi, C, Yang, L. FFEINR: Flow feature-enhanced implicit neural representation for spatio-temporal super-resolution. *arXiv preprint arXiv:230812508* 2023;.
- [11] Dong, C, Loy, CC, He, K, Tang, X. Image super-resolution using deep convolutional networks. *IEEE Transactions on Pattern Analysis and Machine Intelligence* 2016;38(2):295–307.
- [12] Li, Z, Yang, J, Liu, Z, Yang, X, Jeon, G, Wu, W. Feedback network for image super-resolution. In: *Proceedings of IEEE Conference on Computer Vision and Pattern Recognition*. 2019, p. 3862–3871.
- [13] Liang, J, Cao, J, Sun, G, Zhang, K, Van Gool, L, Timofte, R. SwinIR: Image restoration using swin transformer. In: *Proceedings of IEEE Conference on Computer Vision Workshops*. 2021, p. 1833–1844.
- [14] Meyer, S, Wang, O, Zimmer, H, Grosse, M, Sorkine-Hornung, A. Phase-based frame interpolation for video. In: *Proceedings of IEEE Conference on Computer Vision and Pattern Recognition*. 2015, p. 1410–1418.
- [15] Niklaus, S, Mai, L, Liu, F. Video frame interpolation via adaptive separable convolution. In: *Proceedings of IEEE International Conference on Computer Vision*. 2017, p. 261–270.
- [16] Jiang, H, Sun, D, Jampani, V, Yang, MH, Learned-Miller, E, Kautz, J. Super SloMo: High quality estimation of multiple intermediate frames for video interpolation. In: *Proceedings of IEEE Conference on Computer Vision and Pattern Recognition*. 2018, p. 9000–9008.
- [17] Mildenhall, B, Srinivasan, PP, Tancik, M, Barron, JT, Ramamoorthi, R, Ng, R. Nerf: Representing scenes as neural radiance fields for view synthesis. In: *Proceedings of European Conference on Computer Vision*. 2020, p. 405–421.
- [18] Sitzmann, V, Martel, JNP, Bergman, AW, Lindell, DB, Wetzstein, G. Implicit neural representations with periodic activation functions. In: *Proceedings of Advances in Neural Information Processing Systems*. 2020.
- [19] Lu, Y, Jiang, K, Levine, JA, Berger, M. Compressive neural representations of volumetric scalar fields. *Computer Graphics Forum* 2021;40(3):135–146.
- [20] Weiss, S, Hermüller, P, Westermann, R. Fast neural representations for direct volume rendering. *Computer Graphics Forum* 2022;41(6):196–211.
- [21] Han, M, Sane, S, Johnson, CR. Exploratory Lagrangian-based particle tracing using deep learning. *Journal of Flow Visualization and Image Processing* 2022;29(3):73–96.
- [22] Wu, Q, Bauer, D, Doyle, MJ, Ma, KL. Interactive volume visualization via multi-resolution hash encoding based neural representation. *IEEE Transactions on Visualization and Computer Graphics* 2023;Accepted.
- [23] Chen, Z, Chen, Y, Liu, J, Xu, X, Goel, V, Wang, Z, et al. VideoINR: Learning video implicit neural representation for continuous space-time

super-resolution. In: Proceedings of IEEE Conference on Computer Vision and Pattern Recognition. 2022, p. 2037–2047.

[24] Wu, Q, Li, Y, Sun, Y, Zhou, Y, Wei, H, Yu, J, et al. An arbitrary scale super-resolution approach for 3D MR images via implicit neural representation. *IEEE Journal of Biomedical and Health Informatics* 2022;27(2):1004–1015.

[25] Park, JJ, Florence, P, Straub, J, Newcombe, R, Lovegrove, S. DeepSDF: Learning continuous signed distance functions for shape representation. In: Proceedings of IEEE Conference on Computer Vision and Pattern Recognition. 2019, p. 165–174.

[26] Li, T, Slavcheva, M, Zollhöfer, M, Green, S, Lassner, C, Kim, C, et al. Neural 3D video synthesis from multi-view video. In: Proceedings of IEEE Conference on Computer Vision and Pattern Recognition. 2022, p. 5511–5521.

[27] Wu, Q, Bauer, D, Chen, Y, Ma, KL. HyperINR: A fast and predictive hypernetwork for implicit neural representations via knowledge distillation. *arXiv preprint arXiv:230404188* 2023;.

[28] Mehta, I, Gharbi, M, Barnes, C, Shechtman, E, Ramamoorthi, R, Chandraker, M. Modulated periodic activations for generalizable local functional representations. In: Proceedings of IEEE International Conference on Computer Vision. 2021, p. 14194–14203.

[29] Zadeh, A, Lim, YC, Liang, PP, Morency, LP. Variational auto-decoder: A method for neural generative modeling from incomplete data. *arXiv preprint arXiv:190300840* 2019;.

[30] Kingma, DP, Welling, M. Auto-encoding variational Bayes. *arXiv preprint arXiv:13126114* 2013;.

[31] Chen, H, He, B, Wang, H, Ren, Y, Lim, SN, Shrivastava, A. NeRV: Neural representations for videos. In: Proceedings of Advances in Neural Information Processing Systems. 2021, p. 21557–21568.

[32] Aftab, A, Morsali, A, Ghaemmaghami, S. Multi-head ReLU implicit neural representation networks. In: Proceedings of IEEE International Conference on Acoustics, Speech and Signal Processing. 2022, p. 2510–2514.

[33] Wang, C, Ma, KL. A statistical approach to volume data quality assessment. *IEEE Transactions on Visualization and Computer Graphics* 2008;14(3):590–602.

[34] Hawkes, ER, Sankaran, R, Sutherland, JC, Chen, JH. Scalar mixing in direct numerical simulations of temporally evolving plane jet flames with skeletal CO/H₂ kinetics. *Proceedings of the Combustion Institute* 2007;31(1):1633–1640.

[35] Rojo, IB, Günther, T. Vector field topology of time-dependent flows in a steady reference frame. *IEEE Transactions on Visualization and Computer Graphics* 2019;26(1):280–290.

[36] Whalen, D, Norman, ML. Ionization front instabilities in primordial H II regions. *The Astrophysical Journal* 2008;673:664–675.

[37] Popinet, S, Smith, M, Stevens, C. Experimental and numerical study of the turbulence characteristics of airflow around a research vessel. *Journal of Atmospheric and Oceanic Technology* 2004;21(10):1575–1589.

[38] Yüce, G, Ortiz-Jiménez, G, Besbinar, B, Frossard, P. A structured dictionary perspective on implicit neural representations. In: Proceedings of IEEE Conference on Computer Vision and Pattern Recognition. 2022, p. 19206–19216.

[39] Crawfis, RA, Max, N. Texture splats for 3D scalar and vector field visualization. In: Proceedings of IEEE Visualization Conference. 1993, p. 261–267.

[40] Silver, D, Wang, X. Tracking and visualizing turbulent 3D features. *IEEE Transactions on Visualization and Computer Graphics* 1997;3(2):129–141.

[41] Zhang, R, Isola, P, Efros, AA, Shechtman, E, Wang, O. The unreasonable effectiveness of deep features as a perceptual metric. In: Proceedings of IEEE Conference on Computer Vision and Pattern Recognition. 2018, p. 586–595.

[42] Barrow, HG, Tenenbaum, JM, Bolles, RC, Wolf, HC. Parametric correspondence and chamfer matching: Two new techniques for image matching. In: Proceedings of International Joint Conference on Artificial Intelligence. 1977, p. 659–663.

[43] He, W, Wang, J, Guo, H, Wang, KC, Shen, HW, Raj, M, et al. InSituNet: Deep image synthesis for parameter space exploration of ensemble simulations. *IEEE Transactions on Visualization and Computer Graphics* 2019;26(1):23–33.

[44] Shi, N, Xu, J, Li, H, Guo, H, Woodring, J, Shen, HW. VDL-Surrogate: A view-dependent latent-based model for parameter space exploration of ensemble simulations. *IEEE Transactions on Visualization and Computer Graphics* 2022;29(1):820–830.

Appendix

Besides the multi-head and VAD analysis investigated in the paper, we study three parameters influencing STSR-INR training: network depth, latent vector length, and modulator activation function.

Network depth. To determine the optimal network depth, namely, the number of residual blocks d for STSR-INR to achieve the best performance, we conduct a parameter study on the half-cylinder (VTM: 640 and 6400) dataset. The results are presented in Table 1. We observe that for multivariate STSR, the network's generalization capability is crucial in achieving high accuracy. Overfitting becomes a significant issue as d increases beyond five, leading to a big drop in accuracy. On the other hand, when there are no residual blocks, the model suffers from underfitting, as shown in Figure 1. To balance the generalization and fitting capabilities, we utilize five residual blocks for our STSR-INR.

Table 1: Average PSNR (dB), LPIPS, and model size (MB) for STSR-INR with different numbers of residual blocks d for the half-cylinder (VTM: 640 and 6400) dataset. $u_s = 4$ and $u_t = 3$.

d	PSNR \uparrow	LPIPS \downarrow	model
0	36.69	0.215	0.39
5	38.43	0.205	5.41
10	36.53	0.193	10.43

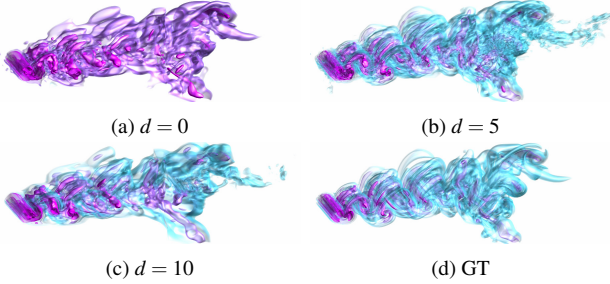


Fig. 1: Network depth: comparing volume rendering of half-cylinder (VTM: 640) dataset. $u_s = 4$ and $u_t = 3$.

Latent vector length. To assess the impact of the latent vector length l , we conduct a parameter study on the Tangaroa (VLM and ACC) dataset. The results are summarized in Table 2. We observe that varying l does not significantly influence the reconstruction result, as shown in Figure 2. Although $l = 1024$ achieves the best result, we find that a length of 256 achieves a similar level of accuracy while utilizing fewer parameters. Therefore, we choose $l = 256$ for our STSR-INR.

Table 2: Average PSNR (dB) and LPIPS for STSR-INR with different latent vector lengths for the Tangaroa (VLM and ACC) dataset. $u_s = 5$ and $u_t = 3$.

latent vector length	PSNR \uparrow	LPIPS \downarrow
64	33.25	0.201
256	33.29	0.199
512	33.27	0.211
1024	33.40	0.226

Modulator activation function. Mehta et al. [1] applied the ReLU activation function for their modulator network. Nevertheless, applying a Sine activation to the modulator network could stabilize network training as the input and output ranges

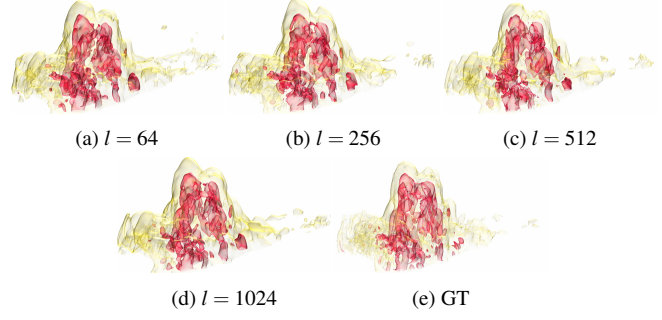


Fig. 2: Latent vector length: comparing volume rendering of the Tangaroa (VLM) dataset. $u_s = 5$ and $u_t = 3$.

in the synthesis network remain $[-1, 1]$. We conduct a comparative study on the ReLU or Sine modulator activation function to demonstrate this. The results shown in Table 3 and Figure 3 suggest that the modulator with Sine activation can achieve a significantly higher reconstruction accuracy than ReLU.

Table 3: Average PSNR (dB) and LPIPS for STSR-INR with different modulator activation functions for the half-cylinder (VTM: 160 and 320). $u_s = 4$ and $u_t = 3$.

activation function	PSNR \uparrow	LPIPS \downarrow
ReLU	27.08	0.039
Sine	41.11	0.015

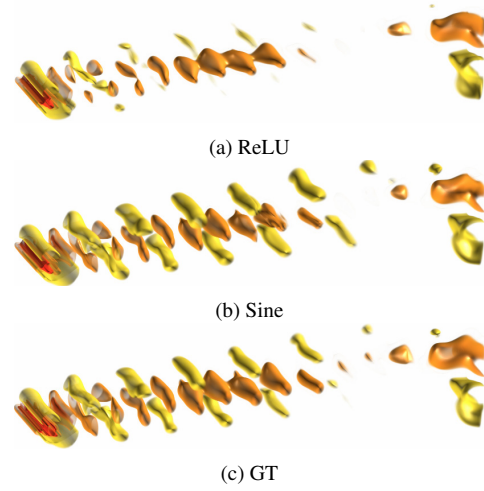


Fig. 3: Modulator activation function: comparing volume rendering of half-cylinder (VTM: 160) dataset. $u_s = 4$ and $u_t = 3$.

References

[1] Mehta, I., Gharbi, M., Barnes, C., Shechtman, E., Ramamoorthi, R., Chandraker, M. Modulated periodic activations for generalizable local functional representations. In: Proceedings of IEEE International Conference on Computer Vision. 2021, p. 14194–14203.